

Article

Open Access

# Active tuning of electromagnetically induced transparency from chalcogenide-only metasurface

Kuan Liu<sup>1</sup>, Meng Lian<sup>1</sup>, Kairong Qin<sup>1</sup>, Shuang Zhang<sup>2</sup> and Tun Cao<sup>1,\*</sup> 

## Abstract

Electromagnetically induced transparency (EIT) is a coherent optical process that provides a narrow transparent peak within a broad absorption line in an atomic medium. All-dielectric metasurface analogues of EIT have enabled new developments in the nanophotonics field for obtaining smaller, more effective slow-light devices and highly sensitive detectors without a quantum approach. However, the dynamic control of the EIT response of all-dielectric metasurfaces has been rarely reported hitherto for the near-infrared (N-IR) region, although a broader range of applications will be enabled by a reconfigurable EIT system. In this study, we realise a chalcogenide (germanium antimony telluride, GST) metasurface, which possesses a dynamically tunable EIT response by optically driving the amorphous-crystalline phase change in the GST medium. Only a few tens of nanometres thick, the nanostructured GST film exhibits Mie resonances that are spectrally modified via laser-induced phase transitions, offering a high relative modulation contrast of 80% in the N-IR region. Moreover, an extreme dispersion that results in the ‘slow light’ behaviour is observed within this transparency ‘window’. Furthermore, the group delay of the N-IR beam switches reversibly under the phase transition. The measurement is consistent with both numerical simulation results and phenomenological modelling. Our work facilitates the development of new types of compact ultrafast N-IR holograms, filtering, and ultrasensitive detectors.

## Introduction

Electromagnetically induced transparency (EIT) is a quantum interference phenomenon that exists in coherently driven three-level atomic systems<sup>1,2</sup> and results in the narrow-band cancellation of absorption in the material. A fascinating property of an EIT medium is its ability to significantly reduce the group velocity of light propagating through a material<sup>3</sup>, thereby enabling EIT-based optical

memories and buffering<sup>4-6</sup>. By mimicking the resonant quantum transitions in an atomic medium, an EIT-like response can be realised in various solid-state systems, including electric circuits<sup>7</sup>, coupled optical resonators<sup>8,9</sup>, and plasmonic metamaterials<sup>10-13</sup>. Compared with EIT in atomic systems, such analogues can avoid complicated experimental setups required for laser stability and low-temperature environment<sup>14,15</sup>. Recently, an EIT analogue using Mie-resonant all-dielectric metasurfaces for engineering light fields with high efficiency has been reported. Such all-dielectric metasurfaces composed of arrays of nanostructured high-refractive-index media simultaneously produce intense electric and magnetic resonances<sup>16,17</sup>. In particular, all-dielectric EIT metasurfaces

Correspondence: Tun Cao (caotun1806@dlut.edu.cn)

<sup>1</sup>School of Optoelectronic Engineering and Instrumentation Science, Dalian University of Technology, Dalian 116024, China

<sup>2</sup>Department of Electrical and Electronic Engineering, University of Hong Kong, Pokfulam Road, Hong Kong, 999077, China

These authors contributed equally: Kuan Liu, Tun Cao

© The Author(s) 2021



**Open Access** This article is licensed under a Creative Commons Attribution 4.0 International License, which permits use, sharing, adaptation, distribution and reproduction in any medium or format, as long as you give appropriate credit to the original author(s) and the source, provide a link to the Creative Commons license, and indicate if changes were made. The images or other third party material in this article are included in the article's Creative Commons license, unless indicated otherwise in a credit line to the material. If material is not included in the article's Creative Commons license and your intended use is not permitted by statutory regulation or exceeds the permitted use, you will need to obtain permission directly from the copyright holder. To view a copy of this license, visit <http://creativecommons.org/licenses/by/4.0/>.

based on a high-index medium such as silicon stripes<sup>18</sup>, oligomer antennae<sup>19</sup>, and asymmetric cut-wire meta-atoms<sup>20,21</sup> have been demonstrated recently in the near-infrared (N-IR) region. It is highly desirable to dynamically manipulate the optical characteristics of meta-devices via external control parameters<sup>22</sup>. All-dielectric metasurfaces that derive their functionality from the intense localised electric and magnetic Mie resonances of a high-index resonator is particularly suitable for achieving this active tunability<sup>23–25</sup>, owing to their optical resonances, which can be engineered on-demand via metasurface design<sup>26</sup>. Although researchers have recently investigated different designs of actively tunable all-dielectric metasurfaces, such as the hybridisation of a Si metasurface with a liquid crystal matrix<sup>26,27</sup>, paired photon absorptance on Si metasurfaces<sup>28,29</sup>, and control of the refractive index via photoexcitation<sup>30</sup>, the dynamically reversible tuning of all-dielectric metasurfaces remains an under-explored field. Hence, all-dielectric metasurfaces, in which ultrafast and reconfigurable control can be realised, should be fabricated. Moreover, the compatibility of current EIT dielectric metasurfaces with ultrafast photonic systems operating with nanosecond pulses and low-power optically modulated switchers remains a formidable challenge.

Chalcogenide phase change materials (PCMs), such as Ge, Sb, and Te, can be repeatedly (up to  $10^{15}$  cycles) and promptly (nanoseconds)<sup>31</sup> transitioned between disordered-amorphous and ordered-crystalline states (and even between intermediate states) via appropriate electrical, thermal, or optical stimuli<sup>32</sup>. Chalcogenide PCMs have been widely applied in electrical memory technologies<sup>33</sup>. Their optical dielectric constants between the amorphous and crystalline states differ significantly<sup>34,35</sup>, rendering them appealing for forming rapid, low-power consumption tunable optical devices<sup>36,37</sup>. Recently, Ge–Sb–Te (GST)-based PCMs have garnered significant interest in the development of active plasmonic meta-devices<sup>38–46</sup>, which deliver various switchable optical functionalities through integration with metal nanostructures, including tunable perfect absorption<sup>47,48</sup>, reconfigurable optical activities<sup>41</sup>, and multispectral imaging<sup>49,50</sup>. Owing to the high refractive index and prominent contrast between structural states within GST, it has recently emerged as a promising paradigm for tunable all-dielectric metasurfaces<sup>51–56</sup>. However, reverse crystalline-to-amorphous state transitions have not been experimentally realised in most GST dielectric metasurfaces<sup>51,54–56</sup>. A few metasurface designs are based on a hybrid of multilayer resonators<sup>53,56</sup>, which render them complicated to fabricate, and some of them have polarisation-dependent optical responses<sup>51,54</sup>. It is noteworthy that dielectric metasurfaces based on patterned

monolithic GST-only films for achieving the dynamic and reversible tuning of an EIT-like response have not yet been realised experimentally.

In this study, we demonstrate the reversible tuning of EIT-like spectra using a GST all-dielectric metasurface possessing magnetic and electric resonances in the N-IR region. The EIT-like resonance was created by coupling between the electric dipolar (ED) and toroidal dipolar (TD) modes<sup>52</sup> and can be optically engineered by changing the complex refractive index ( $n_{\text{GST}}$ ) of GST via its phase transition between amorphous and crystalline states. The all-dielectric metasurface comprised round nanohole arrays (RNAs) embedded in a  $\text{SiO}_2/\text{Ge}_2\text{Sb}_2\text{Te}_5$  (GST225) dual-layer on top of a  $\text{SiO}_2$  substrate, where a 10-nm-thick  $\text{SiO}_2$  layer was used to protect the GST225 against oxidation. The GST225 exhibited a refractive index whose real part ( $\text{Re}(n_{\text{GST}})$ ) was between 4 and 7.2 over a 1000–2200 nm spectral region; this range is much larger than those of typical N-IR dielectrics such as PbTe, Si, and Ge. We exploited this high  $\text{Re}(n_{\text{GST}})$  to design the resonant response in dielectric nanohole metasurfaces, which host complex higher-order modes in the N-IR range. We obtained a broad tuning range of 360 nm and a significant relative modulation contrast of 80% at an EIT resonance of  $\lambda = 1400$  nm by switching the GST225 layer between its amorphous and crystalline phases. To achieve a reconfigurable EIT response, a reversible phase transition of GST225 must be realised. In this study, we reamorphised GST225 using a nanosecond pulsed laser. Finally, we demonstrated that the group delay of the N-IR light can be actively engineered by reversibly switching the state of GST225 between amorphous and crystalline, which provides a practical method for reconfigurable holograms, sensors, and laser beaming devices, while affording advantages of real-time switching, small footprint, simple geometry, and lightweightness.

## Results

### Design and Fabrication

Fig. 1a shows the scheme of our proposed system and the tuning mechanism employed. As a proof-of-concept, we used an all-dielectric metasurface composed of a square array of round nanoholes etched into a  $\text{SiO}_2$  (10 nm thickness)/GST225(60 nm thickness) dual-layer residing on a  $\text{SiO}_2$  substrate (Fig. 1a). The top  $\text{SiO}_2$  layer prevented GST225 from being oxidised. Our proposed all-dielectric EIT metasurface based on GST targets the technologically important N-IR region, which enables highly prominent applications in free-space optical communication and molecular sensing<sup>57–61</sup>. However, the pitch of the meta-

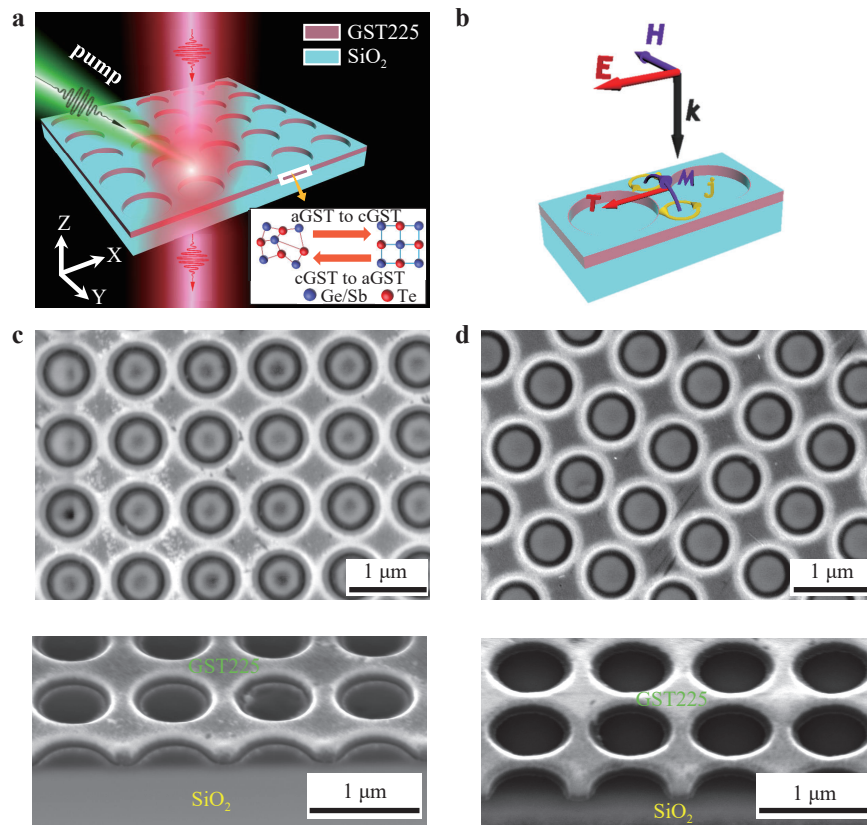


**Fig. 1 Configuration of GST225 all-dielectric metasurface.** **a** Scheme of all-optical, nonvolatile, switchable EIT metasurface, where 1 ns laser pulse reversibly transits GST225 film between amorphous and crystalline states. **b** Illustration of nanoholes array supplemented with mode and current distribution within each nanohole. Excitation of toroidal dipole moment is demonstrated, where  $\vec{M}$  represents magnetic dipole moment,  $\vec{j}$  electric current loops, and  $\vec{T}$  toroidal dipole moment. Geometrical parameters include hole diameter  $d = 700$  nm, metasurface pitch  $p = 900$  nm, and hole depth  $h = 60$  nm. SEM images of GST225 metasurface for **c** amorphous and **d** crystalline states, where top and bottom panels present top and cross-section images of structures. Scale bar: 1  $\mu\text{m}$ .

atoms must be much shorter than the resonant wavelength to avoid high-order diffractions. This results in a miniature resonator that is difficult to obtain experimentally in the N-IR regime, such as a square-like ring combined with nanorods<sup>54</sup>, spheres<sup>62</sup>, double C-shaped resonators<sup>63</sup>, cut wires integrated with split-rings<sup>64</sup>, three cut-outs<sup>65</sup>, and asymmetric paired rods<sup>66</sup>. In this study, the nanoholes were used to replace the complicated resonators owing to the ease of fabrication. Such a circular hole array is simple in terms of geometry. The nanohole array design can improve the uniformity of the meta-atoms during fabrication, thereby affording better performing EIT meta-devices. In this study, the GST225 metasurface allows the simultaneous excitation of ED and TD resonances<sup>67</sup>, where an EIT window can be created via destructive interference between them. The TD moment in the all-dielectric metamaterials is caused by displacement currents ( $\vec{j}$ ), which differs from magnetic resonances in plasmonic metamaterials caused by conduction currents.  $\vec{j}$  assumes the meridian form on the toroidal surface that resembles

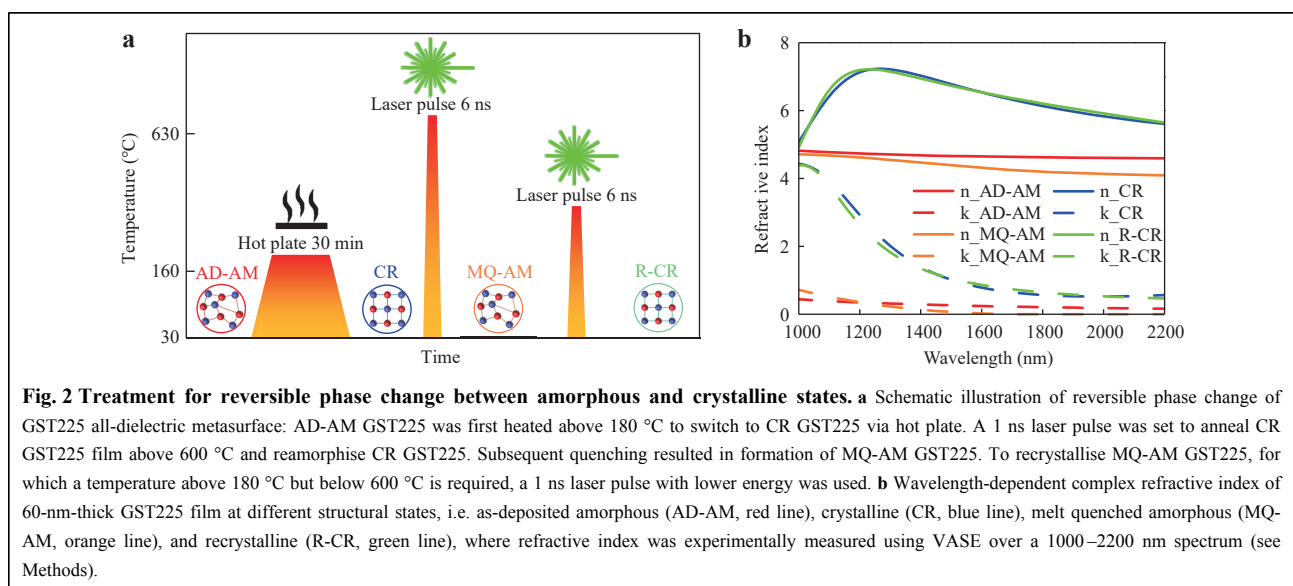
the poloidal currents and produces a magnetic resonance mode confined within the gedanken torus. Such a configuration can create an electromagnetic analogue of the TD moment in all-dielectric metamaterials<sup>68,69</sup>. A schematic illustration of the resonator is shown in Fig. 1b. As shown, the incident wave propagated along the  $z$ -direction, and its electric ( $E$ -) field polarised along the  $x$ -direction. Consequently,  $\vec{j}$  formed two loops of current: clockwise and counterclockwise. These current loops formed a circulated magnetic mode  $\vec{M}$  confined within them. Such a configuration can create a toroidal dipole moment  $\vec{T}$  polarising along the direction of the  $E$ -field of the incident light. The interaction between the toroidal dipole  $\vec{T}$  and electric dipole  $\vec{P}$  modes can yield an EIT resonance mode<sup>70</sup>. Moreover, the interference of strong TD and ED resonances achieved by utilising dielectric resonators enables dynamically and actively reconfigurable EIT meta-devices with high efficiency to be realised. A 60-nm-thick GST225 layer was first deposited on the  $\text{SiO}_2$  substrate via radio frequency (RF) sputtering from GST225 composition

targets. A 10-nm-thick SiO<sub>2</sub> film was deposited directly onto the GST225 film. The RNAs were subsequently milled through the SiO<sub>2</sub>/GST225 dual-layer using a focused ion beam (FIB, FEI Helios NanoLab 600) with a beam current of  $\leq 750$  pA to prevent the crystallisation of GST225 (through ion beam-caused heating) during milling. A flowchart of the entire fabrication process is schematically illustrated in supplementary Fig. S1. A scanning electron microscopy (SEM) image of the as-deposited (AD) amorphous (AM) GST225 metasurface is shown in the top panel of Fig. 1c. The measured lattice constants and diameters were 890 and 690 nm, respectively, which were similar to the designed values (Fig. 1b). The area of the fabricated metasurface was 300  $\mu\text{m} \times 300 \mu\text{m}$ . The cross-sectional SEM image of the metasurface is presented in the bottom panel of Fig. 1c, in which a hole depth of  $\sim 70$  nm that matches the thickness of the SiO<sub>2</sub>/GST225 dual-layer is shown. We crystallised the AD-AM GST225 metasurface by thermally annealing it for 30 min at 180 °C on a hot plate in a flowing Ar atmosphere. Fig. 1d shows that the geometries of the RNAs (top panel) and their cross-sections (bottom panel) were well preserved after the structural phase change of GST225 from amorphous to crystalline.

### Experimental realisation of reversibly tunable EIT

In this study, reversible tuning was achieved via the nanosecond pulsed laser beam. The switching relies on two fundamental phase transitions, i.e. amorphisation and recrystallisation, which occur at different temperatures and time scales<sup>64</sup>. Fig. 2a shows a schematic illustration of the treatment of the GST225 all-dielectric metasurface. First,

we crystallised the AD-AM GST225 film by thermally annealing it at 300 °C, which is above the glass-transition temperature  $T_C = 180$  °C but below the melting temperature  $T_M = 600$  °C, for 30 min on a hot plate in a flowing Ar atmosphere. This process provides a natural switching process that occurs through crystallisation growth and nucleation. Reamorphisation, a melt-quenching process, was achieved by heating GST225 above  $T_M = 600$  °C using an ex situ nanosecond laser pulse excitation, followed by rapid cooling<sup>32,71,72</sup>. The nanosecond laser had a peak intensity (fluence) of 430  $\text{mW}\mu\text{m}^{-2}$  with a central wavelength  $\lambda = 532$  nm, which can yield a numerous electron-hole pairs and melt the GST225. The subsequent fast cooling quenched the melted material into the AM phase (room temperature) at a rate of  $10^9$ – $10^{10}$  K/s, which prevents the recrystallisation of the atomic structure<sup>68</sup>. To recrystallise the melt-quenched (MQ) AM GST225 film, 6 ns laser pulses at  $\lambda = 532$  nm with a decreasing intensity of 215  $\text{mW}\mu\text{m}^{-2}$  were employed to maintain the GST225 above  $T_C = 180$  °C but below  $T_M = 600$  °C. This resulted in a significant contrast in the optical properties between the two different structural states, and this phenomenon has been extensively investigated as a platform for efficient, prompt, nonvolatile, reproducible phase changes. Variable-angle spectroscopic ellipsometry (VASE) was used to characterise the optical properties of the 60-nm-thick GST225 layer for the AD-AM (red line), CR (blue line), MQ-AM (orange line), and recrystalline (R-CR, green line) states in the 1000–2200 nm spectral range, from which we extracted the complex refractive index dispersion (Fig. 2b). The Tauc–Lorentz model was used to fit the real ( $n_{\text{GST}}$ , solid lines) and imaginary ( $k_{\text{GST}}$ , dashed lines) components

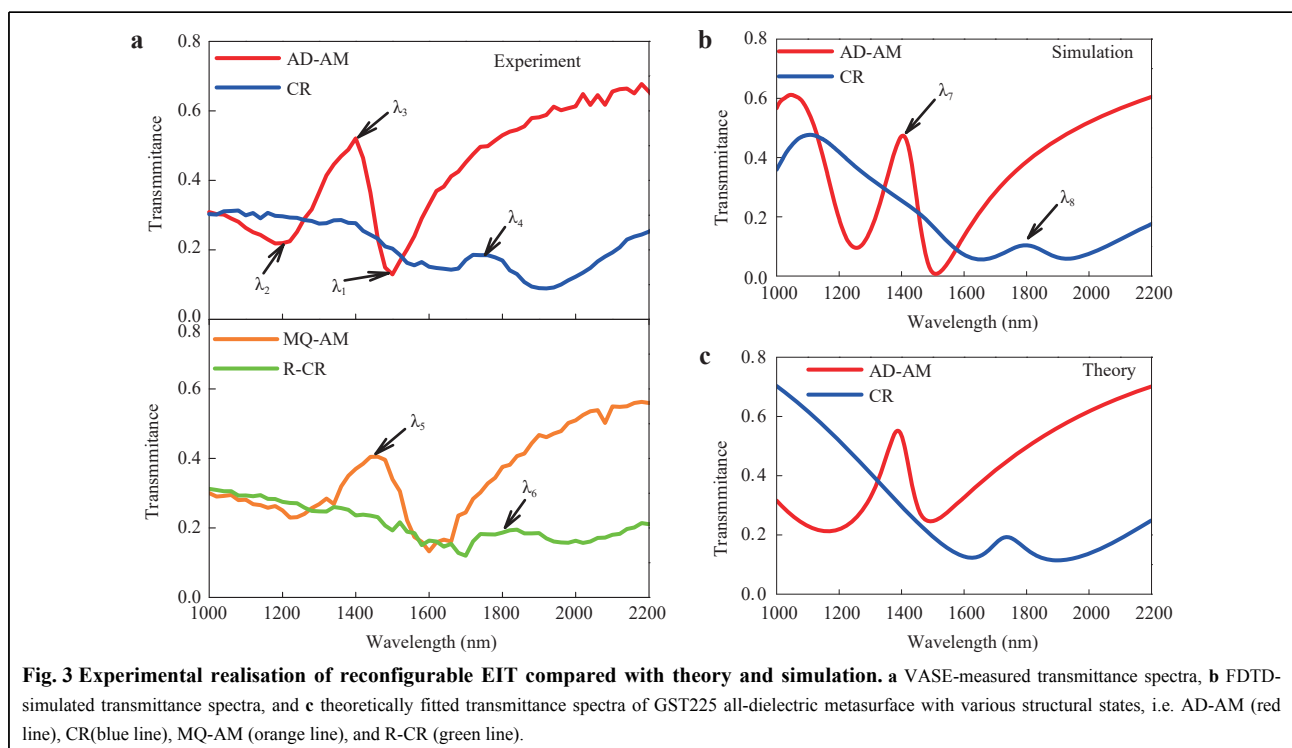


of the complex refractive index ( $N_{\text{GST}} = n_{\text{GST}} + i \times k_{\text{GST}}$ ). The  $n_{\text{GST}}$  changed significantly between the two structural states, resulting in a switchable N-IR resonance that is supported by the RNAs. Overall variations  $\Delta n_{\text{GST}} \sim 3.2$  and  $\Delta k_{\text{GST}} \sim 3.8$  were achieved by changing between predominantly covalent bonds in the AM phase and resonant bonds in the CR phase.

The measured transmittance spectra of the fabricated GST225 dielectric metasurface at different structural states are presented in Fig. 3a. The spectra were segregated into two panels to differentiate between the metasurface treatments, where the top panel shows a spectral comparison of the AD-AM (red solid line) to the annealed CR (blue solid line) phases. By contrast, the bottom panel illustrates the spectra comparison of the MQ-AM (orange solid line) to the R-CR (green solid line) states after a nanosecond-laser-enabled phase change. A detailed discussion of the measurement is presented in the Methods section. For the AD-AM and MQ-AM states, a transmittance dip corresponding to the ED resonance occurred at a wavelength of  $\lambda_1 = 1500$  nm. As expected, a second transmittance dip associated with the TD resonance occurred at a shorter wavelength ( $\lambda_2 = 1220$  nm). An EIT peak appeared between two resonance minima with a peak transmittance of 0.5, at a wavelength of  $\lambda_3 = 1400$  nm. The bottom panel shows the transmittance spectra after the crystallisation of GST225 via either thermal heating (CR)

or laser transition (R-CR). Here, both the ED and TD Mie-like resonances were suppressed, which obliterated the EIT feature at  $\lambda_3 = 1400$  nm. This is because the crystallisation of GST225 significantly increased  $k_{\text{GST}}$ , as shown in Fig. 2b. This results in a high contrast ratio and a relative modulation contrast of  $|T_{\text{AD-AM}} - T_{\text{CR}}|/T_{\text{CR}} = 0.8$  at  $\lambda_3 = 1400$  nm, where  $T_{\text{AD-AM}}$  and  $T_{\text{CR}}$  are the transmissions of the metasurface for the structural states of AD-AM and CR, respectively. Furthermore, the higher  $n_{\text{GST}}$  of the CR state shifted the resonances to longer wavelengths. The resonant wavelength of the peak transmittance red-shifted from  $\lambda_3 = 1400$  nm to  $\lambda_4 = 1760$  nm upon the thermal annealing of the GST225 dielectric from its AD-AM to CR phase (top panel of Fig. 3a). By contrast, a blue shift of the peak resonance from  $\lambda_4 = 1760$  nm (CR) to  $\lambda_5 = 1460$  nm (MQ-AM) and a red-shift from  $\lambda_5 = 1460$  nm (MQ-AM) to  $\lambda_6 = 1800$  nm (R-CR) were optically realised via the nanosecond pulsed laser. The variations in the resonant frequency imply reversible tuning ( $\lambda_3 \rightarrow \lambda_4 \rightarrow \lambda_5$ ), which corresponded to the reamorphisation and recrystallisation of the GST225 layer, respectively. The EIT response of the metasurface with an area of  $40000 \mu\text{m}^2$  can switch between two spectrally separate N-IR channels. The active control of the EIT spectra and dynamic band selectivity in the metasurface represent a significant over passive EIT photonic devices.

To compare the measured results with the theoretical



predictions, we performed a numerical simulation using the finite difference time domain (FDTD) method to solve Maxwell's equations for the metasurface<sup>73</sup>. The simulation data shown in Fig. 3b agree well with the experimental measurements (Fig. 3a). In the model, we employed the VASE-measured refractive index for the GST225 film with different structural states (Fig. 2b) as well as for the geometrical parameters of the metasurface obtained from the SEM images presented in Fig. 1c. The refractive index for the SiO<sub>2</sub> substrate was based on Palik<sup>74</sup>. The transmittance spectra were simulated by illuminating the metasurfaces with a plane wave at normal incidence, as shown in Fig. 1a. A detailed explanation of the model is provided in the Methods section. The reversible tuning of the EIT resonance was numerically observed by altering the structural phase of GST225 between the amorphous and crystalline phases. The profiles of the simulated spectra agreed well with the measurements, although the quality factor of the measurement decreased. A few factors resulted in discrepancies between the simulation and experiment. First, in the ideal model, we did not consider the surface roughness, structural disorder, finite size, and imperfections in the fabricated metasurface (e.g. small over-milling of RNAs into the substrate and stoichiometric variations in the GST225 layer during FIB milling). These aspects can induce additional scattering loss, which consequently decreases the Q-factor and slightly broadens the measured spectra<sup>75,76</sup>. Additionally, gallium contamination during FIB milling may introduce absorption and stoichiometrically modify the nanostructured GST (e.g. decreasing the refractive index caused by irradiation, creation of gallium implantation, and defects)<sup>77,78</sup>. In the experiment, we measured the transmittance spectra of the metasurface in the far-field. In the model, we calculated the spectra in the near-field of the metasurface that introduced variations between the experiment and simulation<sup>79</sup>. Herein, we investigate the physical origin of the active modulation of the EIT response and the near-field coupling effect between the ED and TD resonances in the GST225 meta-atom based on a coupled harmonic Lorentz oscillator model<sup>13</sup>, as follows:

$$\omega_E^{-2}\ddot{m}(t) + \Pi_E\omega_E^{-1}\dot{m}(t) + m(t) = g(t) - \kappa n(t) \quad (1)$$

$$\omega_M^{-2}\ddot{n}(t) + \Pi_M\omega_M^{-1}\dot{n}(t) + n(t) = -\kappa m(t) \quad (2)$$

where  $\omega_E$ ,  $\omega_M$ ,  $\Pi_E$ , and  $\Pi_M$  represent the resonant frequencies and damping rates of the ED and TD resonances, respectively.  $\Pi_E$  and  $\Pi_M$  are expressed by the excitation  $n(t)$  and  $m(t)$  accordingly, and the external driving force  $g(t)$  drives  $\Pi_E$ . The two resonances were linearly coupled with the coupling strength  $\kappa$ . Equations (1)

and (2) are solved in the frequency domain by assuming solution forms of  $m(t) = \tilde{m}(\omega)\exp(-i\omega t)$  and  $n(t) = \tilde{n}(\omega)\exp(-i\omega t)$ , respectively, as follows:

$$\tilde{m}(\omega) = \frac{\Delta_E(\omega)\tilde{g}(\omega)}{\Delta_E(\omega)\Delta_M(\omega) - \kappa^2} \quad (3)$$

$$\tilde{n}(\omega) = \frac{\kappa\tilde{g}(\omega)}{\Delta_E(\omega)\Delta_M(\omega) - \kappa^2} \quad (4)$$

where  $\Delta_{E,M}(\omega) = 1 - (\omega/\omega_{E,M})^2 - i\Pi_{E,M}(\omega/\omega_{E,M})$ . The single resonator of the EIT metasurface can be expressed using an electric current sheet based on the surface conductivity:

$$\sigma_s = \varepsilon_0\chi_s^{(static)} \frac{-i\omega\tilde{m}(\omega)}{\tilde{g}(\omega)} = \frac{-i\omega\beta\Delta_M(\omega)}{\Delta_M(\omega)\Delta_E(\omega) - \kappa^2} \quad (5)$$

where  $\chi_s$  is the surface susceptibility, and  $\beta = \varepsilon_0\chi_s^{(static)}$ . Therefore, the transmittance coefficient of the EIT metasurface can be expressed as

$$T = \frac{2}{2 + \eta_0\sigma_s} \quad (6)$$

where  $\eta_0$  represents the wave impedance in free space.

In Fig. 3c, the measured transmittance spectra of the GST225 metasurface in the amorphous and crystalline states are analytically fitted using Eq. 6; as shown, they agree reasonably well with both the measured (top panel of Fig. 3a) and simulated (Fig. 3b) data. The fitting parameters for,  $\omega_E$ ,  $\omega_M$ ,  $\Pi_E$ ,  $\Pi_M$ , and  $\kappa$  are listed in Table S1 in the Supplementary Information. As shown, the damping rate of the TD mode  $\Pi_M$  increased significantly (i.e. by two orders of magnitude) for the CR state, indicating that the phase transition of GST225 changed the resonant strength of the TD mode. Therefore, the active tuning of the EIT resonance was due to the difference in  $\Pi_M$ . In the AM-GST225 metasurface with a low  $\Pi_M$ , the two pathways interfered destructively to generate a sharp EIT transmittance peak. However, by crystallising the GST225 layer, the loss in the resonator increased, which suppressed the excitation of the TD mode and removed the EIT resonant peak. Such an EIT response can be reversibly activated by reamorphising the metasurface.

### Resonance modes in EIT metasurface with different structural states

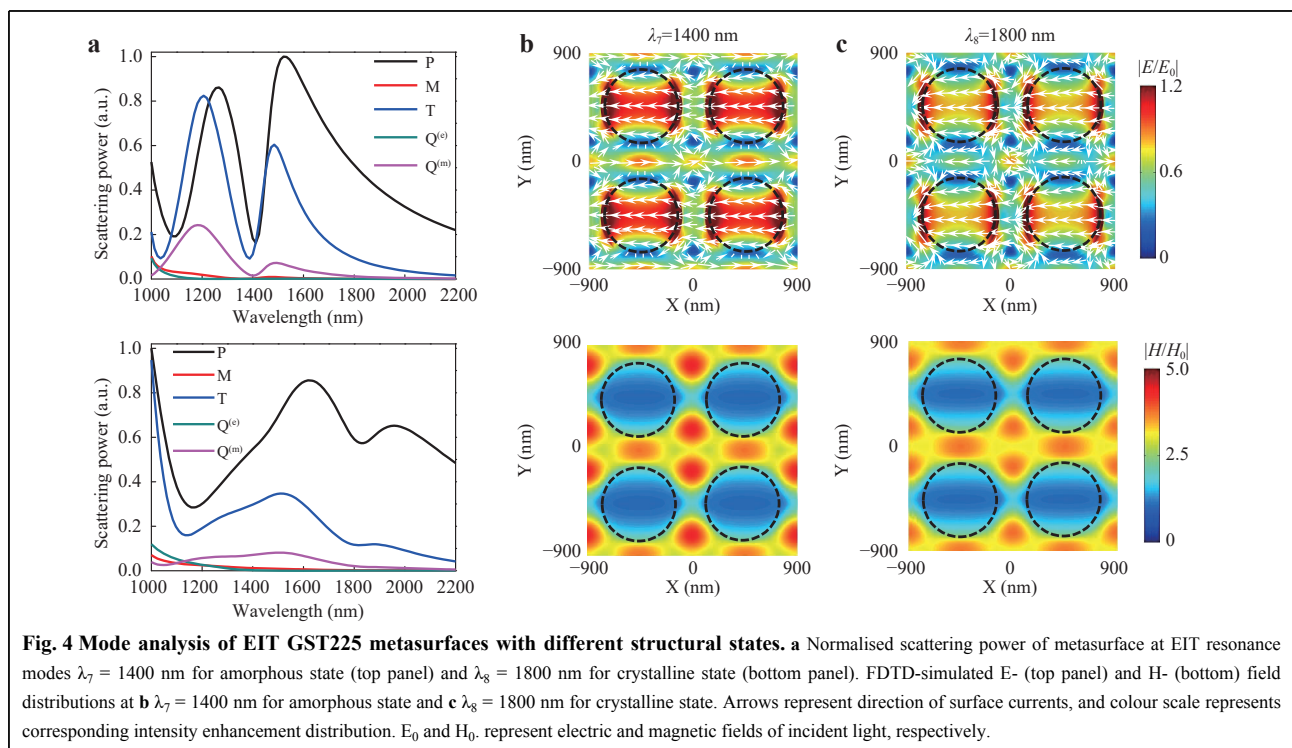
Fig. 3 shows that our proposed GST225 metasurface can realise the dynamic and reversible tuning of the ED and TD resonances, resulting in a reconfigurable EIT response. The fundamental mechanism of such behaviour can be investigated by analysing the mode decomposition and scrutinising the near-field distributions of the metasurface at the ED and TD Mie-type resonances for the different

GST225 states. To investigate the nature of the induced modes, we performed multipole decomposition to evaluate the Cartesian multipole contributions to the scattering for a single nanohole. The five multipole moments depended on the current density distribution inside the nanohole<sup>80</sup> (see the detailed discussion in the Supplementary Information). The multipole decompositions of the EIT resonant modes  $\lambda_7 = 1400$  nm and  $\lambda_8 = 1800$  nm (Fig. 3b) for both the amorphous and crystalline states are shown in the top and bottom panels of Fig. 4a, respectively. As shown, both the electric dipole and toroidal dipole moments contributed significantly to the EIT resonances, whereas the other multipole components ( $\vec{M}$ ,  $\vec{Q}^{(e)}$ ,  $\vec{Q}^{(m)}$ ) were suppressed. Namely, a significant interaction occurred between the toroidal dipole  $\vec{T}$  and electric dipole  $\vec{P}$ , which established the EIT resonant mode. Such dominant contributions of  $\vec{P}$  and  $\vec{T}$  moments were similarly verified in the electromagnetic field distributions at resonant wavelengths of  $\lambda_7 = 1400$  nm and  $\lambda_8 = 1800$  nm, as shown in Fig. 4b, c for the amorphous and crystalline states, respectively. To further investigate the synergistic action of  $\vec{P}$  and  $\vec{T}$  moments in exciting the EIT response, we characterised the total  $E$ -field enhancement and  $\vec{j}$  distributions at  $\lambda_7 = 1400$  nm for the all-dielectric metasurface with AM-GST225, as presented in the top panel of Fig. 4b. As shown, two circular currents ( $E$ -field loops) were excited in the opposite orientation in the  $x$ - $y$  plane near each nanohole,

yielding a magnetic dipole oscillation along the  $z$ -axis. This resulted in a  $\vec{T}$  moment along the  $x$ -axis. Moreover, the  $\vec{P}$  moment along the  $x$ -axis was excited. This indicates that the EIT resonant mode originated from the destructive interaction between the electric dipole and toroidal dipole moments. Substantial  $E$ -field enhancement occurred inside the nanohole, where a more significant enhancement in the total  $E$ -field was observed at four sidelobes around the nanohole, primarily near the electric vortex. The bottom panel shows the total  $H$ -field enhancement distribution at  $\lambda_7 = 1400$  nm. In Fig. 4c, we show the total  $E$ -field (top panel) and  $H$ -field (bottom panel) distributions, respectively, at  $\lambda_8 = 1800$  nm for the crystalline phase. It was discovered that the electromagnetic-field distributions of the structure were similar to those for the amorphous state, which indicates that the electrical and toroidal dipole moments were concurrently excited to yield the EIT response. Our strategy provides excellent flexibility in realising a high-efficiency reconfigurable EIT metasurface. For instance, the interference between the electrical and toroidal dipole resonances in our GST225 metasurface can selectively enhance or suppress the backscattered radiation at a particular wavelength by switching the structural state between amorphous and crystalline.

### Tunable group index

The EIT response in an atomic system can yield a slow-



light effect, which benefits applications in optical memory and quantum memory<sup>81</sup>. In particular, the active modulation of slow light can fulfil future controllable and densely integrated optical devices, such as slow light buffers. Herein, the slow-light feature is characterised by the group index  $n_g$  of the N-IR light transmitted through the EIT metasurface, and  $n_g$  can be extracted from simulations of the transmission and reflection coefficients using a well-established retrieval algorithm<sup>82,83</sup>, as follows:

$$n_g = \frac{c}{v_g} = \frac{c}{L} \tau_g = \frac{c}{L} \frac{d\varphi}{d\omega} \quad (7)$$

where  $c$  represents the speed of light in vacuum,  $L$  the propagation distance of light in the metasurface,  $\tau_g$  the optical delay time,  $\omega$  the angular frequency, and  $\varphi$  the phase shift of the transmission. Here,  $\tau_g = \frac{d\varphi}{d\omega}$  is defined as the ratio of the derived  $\varphi$  to the angular frequency  $\omega$ . Fig. 5a, b present the spectra of  $n_g$  and  $\varphi$  for the proposed GST225 metasurfaces at different structural

states, respectively, using the Lumerical FDTD simulation. Here,  $\varphi$  can be calculated using the transmission coefficient. The dispersion of the light wave becomes strong when the frequency approaches the transparent window. Subsequently, a significant shift in the phase (Fig. 5b) induced by the intense interference yields a considerable change in  $n_g$  (Fig. 5a). For the amorphous GST225 metasurfaces, the maximum  $n_g$  of 335 was obtained at the dip wavelength of  $\lambda_0 = 1500$  nm, indicating that the light wave propagating through the metasurface possessed a group velocity ( $v_g$ ) that was 335 times slower than that in vacuum. Hence, the amorphous GST225 metasurface exhibited a slow-light effect. However,  $n_g$  can be decreased significantly at  $\lambda_0 = 1500$  nm by changing the state of GST225 from amorphous to crystalline. Hence, we can dynamically tune  $n_g$  via the phase transition of GST225. Furthermore, the reversible active tuning of  $n_g$  may result in optically controllable slow-light meta-devices.

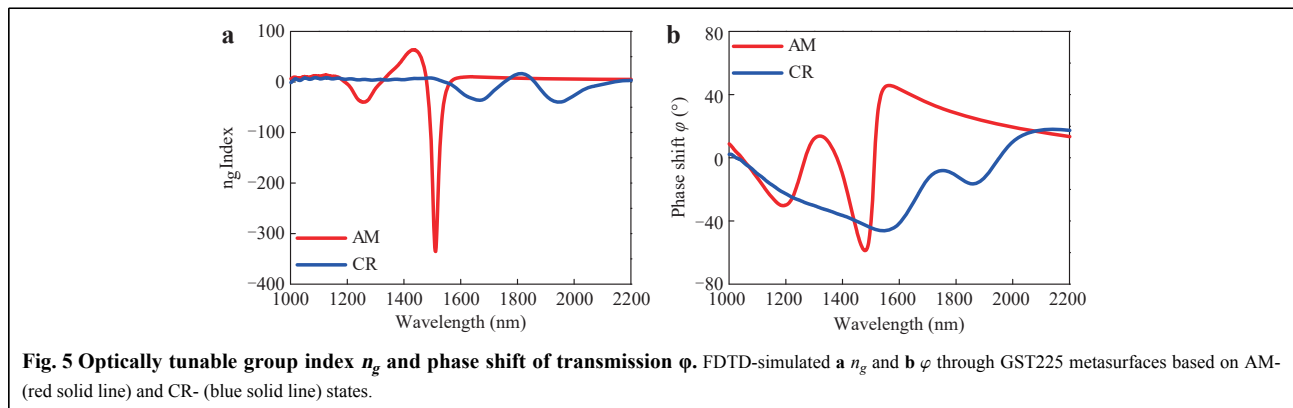


**Fig. 5** Optically tunable group index  $n_g$  and phase shift of transmission  $\varphi$ . FDTD-simulated **a**  $n_g$  and **b**  $\varphi$  through GST225 metasurfaces based on AM- (red solid line) and CR- (blue solid line) states.

## Conclusions

In summary, we designed and experimentally realised an all-optical and reconfigurable EIT metasurface by tuning the spectral positions of ED and TD Mie-type resonances via the phase transition of GST225, achieved via external nanosecond laser pumping. The phase change of GST225 yielded a significant contrast in the effective refractive index and enabled a resonant wavelength shift of  $\sim 360$  nm in the N-IR region, where an experimental transmission relative modulation contrast of up to 80% at  $\lambda_3 = 1400$  nm was achieved. Although the EIT metasurface indicated strong optical modulation, our scheme involving the reversible optical switching of an all-dielectric metasurface based on GST is a general scheme that can be used in various applications. In particular, when combined with structured pumping light illumination, an appropriately

designed metasurface can serve as an active metasurface for dynamic control over the wavefront of N-IR light. This can be potentially used in dynamic optical holography, active lenses, and ultrasensitive sensors.

## Materials and methods

### Sample fabrication

Prior to deposition, a  $\text{SiO}_2$  wafer was selected as the substrate; it was ultrasonically cleaned using acetone, rinsed in isopropyl alcohol, and dried with dry nitrogen. Subsequently, a 60-nm-thick GST225 layer was sputter deposited on top of the  $\text{SiO}_2$  substrate via RF magnetron sputtering. A 99.99% pure GST sputtering target with a diameter of 50.8 mm was deposited at a rate of 0.8 Å/s via 30 W of RF power. Subsequently, a  $\sim 10$ -nm-thick  $\text{SiO}_2$

protection layer was deposited above the GST225 film at a deposition rate of  $0.3 \text{ \AA s}^{-1}$ . We fabricated the metasurfaces using an FEI Helios G4 UX FIB equipped with a Cobra FIB column and a five-channel gas injection system, where a Ga<sup>+</sup> ion beam with a current of 750 pA and an acceleration voltage of 30 keV was used. The step size was set to 10 nm, which provided an excellent overlap between two consecutive spots.

### Sample Measurements

An infrared variable angle spectroscopic ellipsometer integrated with the focusing probes was used to measure the transmittance spectra of the metasurface. The focusing probes can reduce the beam diameter on the sample from 4 mm to 200  $\mu\text{m}$  to adapt to the area of the fabricated metasurface (300  $\mu\text{m} \times 300 \mu\text{m}$ ). The numerical aperture of the lens of the focusing probe was  $\sim 0.01$ . The range of angles at which the structure was simultaneously excited was  $0^\circ\text{--}3^\circ$ . The refractive indices of GST were measured via VASE. A Tauc–Lorentz model was employed to fit the VASE-measured data<sup>42</sup>, thereby minimising the mean square error (MSE) of the fitting procedure ( $\text{MSE} < 6$ )<sup>84</sup>.

### FDTD Simulations

We performed a numerical simulation of the metasurfaces using a commercially available FDTD solver (Lumerical Solutions). We adopted periodic boundary conditions in the plane ( $x\text{--}y$  plane) normal to the incident wave. Perfectly matched layer boundary conditions were applied along the vertical direction ( $z$ -axis) to terminate the simulation. We illuminated the metasurfaces vertically using a plane wave and placed a power monitor 200 nm behind the metasurface to collect the transmitted data. The structure was organised in a uniform cubic grid (2 nm  $\times$  2 nm  $\times$  2 nm), which can eliminate numerical errors. Namely, we adopted a cubic Yee cell with  $\Delta x = \Delta y = \Delta z = 2 \text{ nm}$ , and a time step  $\Delta t = 1 \times 10^{-18} \text{ s}$  to satisfy the Courant stability<sup>85,86</sup>. In the models, the parameters for SiO<sub>2</sub> was based on Palik, losses were not considered in the experimental dielectric constants, and GST225 was determined based on its complex refractive index measured via VASE.

### Acknowledgements

T.C. acknowledges support from the National Key Research and Development Program of China (2020YFA0714504, 2019YFA0709100). Tun Cao and Kuan Liu contributed equally to this study.

### Author contributions

T.C. initiated the study and provided guidance. T. C., S. Z., K. R. Q., and K. L. discussed and wrote the manuscript. M.L. and K.L. conducted the simulations and analysed the data. K.L. performed the measurements. T.C. and K.L. contributed equally to this study.

### Data availability

The data that support the plots presented herein and other findings of this study are available from the corresponding author upon request.

### Code availability

All codes that support this study are available from the corresponding author upon request.

### Conflict of interest

The authors declare that they have no conflicts of interest.

**Supplementary information** is available for this paper at <https://doi.org/10.37188/lam.2021.019>.

Received: 15 March 2021 Revised: 08 July 2021 Accepted: 16 July 2021

Accepted article preview online: 19 July 2021

Published online: 18 September 2021

### References

- Harris, S.E. Electromagnetically Induced Transparency. *Physics Today* **50**, 36–42 (1997).
- Novikova, I., Walsworth, R.L. & Xiao, Y. Electromagnetically induced transparency-based slow and stored light in warm atoms. *Laser & Photonics Reviews* **6**, 333–353 (2012).
- Hau, L.V. et al. Light speed reduction to 17 metres per second in an ultracold atomic gas. *Nature* **397**, 594–598 (1999).
- Vudyasetu, P.K., Camacho, R.M. & Howell, J.C. Storage and retrieval of multimode transverse images in hot atomic rubidium vapor. *Physical review letters* **100**, 123903 (2008).
- Shuker, M. et al. Storing images in warm atomic vapor. *Physical review letters* **100**, 223601 (2008).
- Heinze, G., Hubrich, C. & Halfmann, T. Stopped light and image storage by electromagnetically induced transparency up to the regime of one minute. *Physical review letters* **111**, 033601 (2013).
- Garrido Alzar, C., Martinez, M. & Nussenzevig, P. Classical analog of electromagnetically induced transparency. *American Journal of Physics* **70**, 37–41 (2002).
- Xu, Q. et al. Experimental realization of an on-chip all-optical analogue to electromagnetically induced transparency. *Physical review letters* **96**, 123901 (2006).
- Yang, X. et al. All-optical analog to electromagnetically induced transparency in multiple coupled photonic crystal cavities. *Physical review letters* **102**, 173902 (2009).
- Zhang, S. et al. Plasmon-induced transparency in metamaterials. *Physical review letters* **101**, 047401 (2008).
- Liu, N. et al. Plasmonic analogue of electromagnetically induced transparency at the Drude damping limit. *Nature materials* **8**, 758–762 (2009).
- Kekatpure, R.D. et al. Phase-coupled plasmon-induced transparency. *Physical review letters* **104**, 243902 (2010).
- Kim, T.-T. et al. Electrically tunable slow light using graphene metamaterials. *ACS Photonics* **5**, 1800–1807 (2018).
- Singh, R. et al. Coupling between a dark and a bright eigenmode in a terahertz metamaterial. *Physical Review B* **79**, 085111 (2009).
- Chiam, S.-Y. et al. Analogue of electromagnetically induced transparency in a terahertz metamaterial. *Physical Review B* **80**, 153103 (2009).
- Moitra, P. et al. Realization of an all-dielectric zero-index optical metamaterial. *Nature Photonics* **7**, 791–795 (2013).
- Yang, Y. et al. Dielectric meta-reflectarray for broadband linear

- polarization conversion and optical vortex generation. *Nano letters* **14**, 1394-1399 (2014).
18. Fan, P. et al. Optical Fano resonance of an individual semiconductor nanostructure. *Nature materials* **13**, 471-475 (2014).
  19. Miroshnichenko, A.E. & Kivshar, Y.S. Fano resonances in all-dielectric oligomers. *Nano letters* **12**, 6459-6463 (2012).
  20. Wu, C. et al. Spectrally selective chiral silicon metasurfaces based on infrared Fano resonances. *Nature communications* **5**, 1-9 (2014).
  21. Zhang, J., MacDonald, K.F. & Zheludev, N.I. Near-infrared trapped mode magnetic resonance in an all-dielectric metamaterial. *Optics express* **21**, 26721-26728 (2013).
  22. Nematı, A. et al. Tunable and reconfigurable metasurfaces and metadevices. *Opto-Electronic Advances* **1**, 180009 (2018).
  23. Mie, G. Beiträge zur Optik trüber Medien, speziell kolloidaler Metallösungen. *Annalen der physik* **330**, 377-445 (1908).
  24. Evlyukhin, A.B. et al. Demonstration of magnetic dipole resonances of dielectric nanospheres in the visible region. *Nano letters* **12**, 3749-3755 (2012).
  25. Tian, J. et al. Near-Infrared Super-Absorbing All-Dielectric Metasurface Based on Single-Layer Germanium Nanostructures. *Laser & Photonics Reviews* **12**, 1800076 (2018).
  26. Komar, A. et al. Electrically tunable all-dielectric optical metasurfaces based on liquid crystals. *Applied Physics Letters* **110**, 071109 (2017).
  27. Sautter, J. et al. Active tuning of all-dielectric metasurfaces. *ACS nano* **9**, 4308-4315 (2015).
  28. Shcherbakov, M.R. et al. Ultrafast all-optical switching with magnetic resonances in nonlinear dielectric nanostructures. *Nano letters* **15**, 6985-6990 (2015).
  29. Yang, Y. et al. Nonlinear Fano-resonant dielectric metasurfaces. *Nano letters* **15**, 7388-7393 (2015).
  30. Makarov, S. et al. Tuning of magnetic optical response in a dielectric nanoparticle by ultrafast photoexcitation of dense electron-hole plasma. *Nano letters* **15**, 6187-6192 (2015).
  31. Loke, D. et al. Breaking the speed limits of phase-change memory. *Science* **336**, 1566-1569 (2012).
  32. Wuttig, M. & Yamada, N. Phase-change materials for rewritable data storage. *Nature materials* **6**, 824-832 (2007).
  33. Bakan, G. et al. Extracting the temperature distribution on a phase-change memory cell during crystallization. *Journal of Applied Physics* **120**, 164504 (2016).
  34. Shportko, K. et al. Resonant bonding in crystalline phase-change materials. *Nature materials* **7**, 653-658 (2008).
  35. Ahmadvand, A. et al. Optical switching using transition from dipolar to charge transfer plasmon modes in Ge 2 Sb 2 Te 5 bridged metallodielectric dimers. *Scientific reports* **7**, 1-8 (2017).
  36. Zhu, W. et al. Realization of a near-infrared active Fano-resonant asymmetric metasurface by precisely controlling the phase transition of Ge 2 Sb 2 Te 5. *Nanoscale* **12**, 8758-8767 (2020).
  37. Gerislioglu, B. et al. The role of Ge2Sb2Te5 in enhancing the performance of functional plasmonic devices. *Materials Today Physics* **12**, 100178 (2020).
  38. Michel, A.-K.U. et al. Using low-loss phase-change materials for mid-infrared antenna resonance tuning. *Nano letters* **13**, 3470-3475 (2013).
  39. Michel, A.-K.U. et al. Reversible optical switching of infrared antenna resonances with ultrathin phase-change layers using femtosecond laser pulses. *Acs Photonics* **1**, 833-839 (2014).
  40. Michel, A.K.U. et al. Advanced Optical Programming of Individual Meta-Atoms Beyond the Effective Medium Approach. *Advanced Materials* **31**, 1901033 (2019).
  41. Michel, A.K.U. et al. The Potential of Combining Thermal Scanning Probes and Phase-Change Materials for Tunable Metasurfaces. *Advanced Optical Materials* **9**, 2001243 (2021).
  42. Sreekanth, K.V., Han, S. & Singh, R. Ge2Sb2Te5-Based Tunable Perfect Absorber Cavity with Phase Singularity at Visible Frequencies. *Advanced Materials* **30**, 1706696 (2018).
  43. Sreekanth, K.V. et al. Phase-change-material-based low-loss visible-frequency hyperbolic metamaterials for ultrasensitive label-free biosensing. *Advanced Optical Materials* **7**, 1900081 (2019).
  44. Sreekanth, K.V. et al. Electrically Tunable Singular Phase and Goos-Hänchen Shifts in Phase-Change-Material-Based Thin-Film Coatings as Optical Absorbers. *Advanced Materials* **33**, 2006926 (2021).
  45. Pitchappa, P. et al. Volatile ultrafast switching at multilevel nonvolatile states of phase change material for active flexible terahertz metadevices. *Advanced Functional Materials* **200**(2021), (2100).
  46. Pitchappa, P. et al. Chalcogenide phase change material for active terahertz photonics. *Advanced Materials* **31**, 1808157 (2019).
  47. Cao, T. et al. Mid-infrared tunable polarization-independent perfect absorber using a phase-change metamaterial. *JOSA B* **30**, 1580-1585 (2013).
  48. Qu, Y. et al. Dynamic Thermal Emission Control Based on Ultrathin Plasmonic Metamaterials Including Phase-Changing Material GST. *Laser & Photonics Reviews* **11**, 1700091 (2017).
  49. Cao, T. et al. Tuneable thermal emission using chalcogenide metasurface. *Advanced Optical Materials* **6**, 1800169 (2018).
  50. Gholipour, B. et al. An all-optical, nonvolatile, bidirectional, phase-change meta-switch. *Advanced materials* **25**, 3050-3054 (2013).
  51. Karvounis, A. et al. All-dielectric phase-change reconfigurable metasurface. *Applied Physics Letters* **109**, 051103 (2016).
  52. Chu, C.H. et al. Active dielectric metasurface based on phase-change medium. *Laser & Photonics Reviews* **10**, 986-994 (2016).
  53. de Galarreta, C.R. et al. Reconfigurable multilevel control of hybrid all-dielectric phase-change metasurfaces. *Optica* **7**, 476-484 (2020).
  54. Petronijevic, E. & Sibilia, C. All-optical tuning of EIT-like dielectric metasurfaces by means of chalcogenide phase change materials. *Optics express* **24**, 30411-30420 (2016).
  55. Tian, J. et al. Active control of anapole states by structuring the phase-change alloy Ge 2 Sb 2 Te 5. *Nature communications* **10**, 1-9 (2019).
  56. Leitis, A. et al. All-Dielectric Programmable Huygens' Metasurfaces. *Advanced Functional Materials* **30**, 1910259 (2020).
  57. Agrawal, G.P. Fiber-optic communication systems (John Wiley & Sons, 2012).
  58. Agrawal, G.P. in *Nonlinear Science at the Dawn of the 21st Century* 195-211 (Springer, 2000).
  59. Stanley, R. Plasmonics in the mid-infrared. *Nature Photonics* **6**, 409-411 (2012).
  60. Yin, X. et al. Active chiral plasmonics. *Nano letters* **15**, 4255-4260 (2015).
  61. Tittl, A. et al. A switchable mid-infrared plasmonic perfect absorber with multispectral thermal imaging capability. *Advanced Materials* **27**, 4597-4603 (2015).
  62. Yannopapas, V., Paspalakis, E. & Vitanov, N.V. Electromagnetically induced transparency and slow light in an array of metallic nanoparticles. *Physical Review B* **80**, 035104 (2009).
  63. Kindness, S.J. et al. Active control of electromagnetically induced transparency in a terahertz metamaterial array with graphene for continuous resonance frequency tuning. *Advanced Optical Materials* **6**, 1800570 (2018).
  64. Gu, J. et al. Active control of electromagnetically induced transparency analogue in terahertz metamaterials. *Nature communications* **3**, 1-6 (2012).
  65. Liu, N. et al. Planar metamaterial analogue of electromagnetically induced transparency for plasmonic sensing. *Nano letters* **10**, 1103-1107 (2010).
  66. Abujetas, D.R. et al. Spectral and temporal evidence of robust photonic

- bound states in the continuum on terahertz metasurfaces. *Optica* **6**, 996-1001 (2019).
67. Ospanova, A.K., Stenishchev, I.V. & Basharin, A.A. Anapole mode sustaining silicon metamaterials in visible spectral range. *Laser & Photonics Reviews* **12**, 1800005 (2018).
  68. Zhou, C. et al. Multiple toroidal dipole Fano resonances of asymmetric dielectric nanohole arrays. *Physical Review B* **100**, 195306 (2019).
  69. JunáHe, X. & HuiáZhao, C. A low-loss electromagnetically induced transparency (EIT) metamaterial based on coupling between electric and toroidal dipoles. *RSC advances* **7**, 55897-55904 (2017).
  70. Fedotov, V.A. et al. Resonant transparency and non-trivial non-radiating excitations in toroidal metamaterials. *Scientific reports* **3**, 1-5 (2013).
  71. Raoux, S. Phase change materials. *Annual Review of Materials Research* **39**, 25-48 (2009).
  72. Terao, M., Morikawa, T. & Ohta, T. Electrical phase-change memory: fundamentals and state of the art. *Japanese Journal of Applied Physics* **48**, 080001 (2009).
  73. FDTD. Solutions. at <http://www.lumerical.com>.
  74. Palik, E.D. Handbook of optical constants of solids (Academic press, 1998).
  75. Yuan, S. et al. Strong photoluminescence enhancement in all-dielectric Fano metasurface with high quality factor. *ACS nano* **11**, 10704-10711 (2017).
  76. Mikheeva, E. et al. Photosensitive chalcogenide metasurfaces supporting bound states in the continuum. *Optics Express* **27**, 33847-33853 (2019).
  77. Siegrist, T. et al. Disorder-induced localization in crystalline phase-change materials. *Nature materials* **10**, 202-208 (2011).
  78. San-Román-Alerigi, D.P. et al. Electron irradiation induced reduction of the permittivity in chalcogenide glass (As<sub>2</sub>S<sub>3</sub>) thin film. *Journal of Applied Physics* **113**, 044116 (2013).
  79. Dong, W. et al. Tunable mid-infrared phase-change metasurface. *Advanced Optical Materials* **6**, 1701346 (2018).
  80. Wu, P.C. et al. Optical anapole metamaterial. Optical anapole metamaterial. *ACS nano* **12**, 1920-1927 (2018).
  81. Liu, C. et al. Observation of coherent optical information storage in an atomic medium using halted light pulses. *Nature* **409**, 490-493 (2001).
  82. Lu, H., Liu, X. & Mao, D. Plasmonic analog of electromagnetically induced transparency in multi-nanoresonator-coupled waveguide systems. *Physical Review A* **85**, 053803 (2012).
  83. Chen, X. et al. Robust method to retrieve the constitutive effective parameters of metamaterials. *Physical review E* **70**, 016608 (2004).
  84. Hawlová, P. et al. Photostability of pulsed laser deposited amorphous thin films from Ge-As-Te system. *Scientific reports* **5**, 1-7 (2015).
  85. Yee, K. Numerical solution of initial boundary value problems involving Maxwell's equations in isotropic media. *IEEE Transactions on antennas and propagation* **14**, 302-307 (1966).
  86. Zheng, F., Chen, Z. & Zhang, J. A finite-difference time-domain method without the Courant stability conditions. *IEEE Microwave and Guided wave letters* **9**, 441-443 (1999).